CONFERENCE PRE-PRINT

FUEL SUPPLY AND HELIUM ASH EXHAUST IN GLOBAL GYROKINETIC ITG/TEM TURBULENCE

K. IMADERA

Graduate School of Energy Science, Kyoto University

Email: imadera.kenji.7z@kyoto-u.ac.jp

Y. KISHIMOTO and A. ISHIZAWA Graduate School of Energy Science, Kyoto University

Abstract

Gyrokinetic flux-driven ITG/TEM simulations is performed to study the balance of fuel supply and helium ash exhaust in tokamaks. It is found that the temperature ratio of helium to bulk ion, i.e. T_{He0}/T_{i0} is one of the parameters to control both fuel supply and helium ash exhaust. For thermalized helium $T_{He0}/T_{i0}=1$, clear turbulent particle pinch of bulk ion is observed, while turbulent net particle flux of helium is relatively small. On the other hand, for non-thermalized helium $T_{He0}/T_{i0}=4$, such a turbulent particle pinch of bulk ion is found to be weakened and helium ash accumulation occurs because turbulent particle flux of helium by non-axisymmetric radial drift tends to become negative. This means that hot helium can prevent both fuel supply and helium ash exhaust.

1. INTRODUCTION

Establishment of a refueling method is an important issue for controlling nuclear fusion reactors. But, in DEMO-class high-temperature plasmas, a pellet injection reaches only up to 80%–90% of the minor radius so that the central density peaking depends on particle pinch, making the prediction difficult. It is known that turbulent particle flux consists of a diagonal diffusion term, a non-diagonal thermo-diffusion term, and a convection term. The first term is usually positive for the peaked profile, while the second term can be negative, indicating that it can drive particle pinch. According to the quasi-linear fluid theory [1], the thermo-diffusion coefficient is estimated as $D_T \propto -(10L_n/3R_0 - \omega_r/\omega_{*e})$ so that the sign depends on the real frequency of dominant mode ω_r , the typical scale length of density gradient L_n , the major radius R_0 , and the diamagnetic electron frequency ω_{*e} . In the Ion-Temperature-Gradient (ITG) case, D_T is always negative because the real frequency is negative, while it can be reversed in the Trapped-Electron-Mode (TEM) case. In fact, the turbulent electron particle flux calculated by GS2 simulations shows the opposite trend for electron temperature gradient between ITG and TEM [2, 3].

In addition, recent full-f gyrokinetic simulations suggest the importance of global effects in evaluating impurity particle transport [4] such as core Helium ash exhaust and edge impurity accumulation. For instance, GYSELA full-f gyrokinetic simulations show that the turbulence-driven Reynolds stress causes (m, n) = (1,0) mode, leading to an impact on neoclassical impurity transport in a deuterium plasma with helium, neon, or tungsten as tracer impurities [5]. GT5D full-f gyrokinetic simulations also show that neoclassical impurity transport is enhanced by a turbulent transport driven ambipolar radial electric field in a deuterium plasma with helium, beryllium, carbon, or argon as tracer impurities [6]. These simulations suggest that the interaction between turbulent and neoclassical transport is important for impurity transport, however, the role of the interaction on the particle pinch of bulk ion has not been investigated yet.

Based on such a motivation, we performed flux-driven ITG/TEM simulations in the presence of ion/electron heating [7] by means of the full-f electrostatic version of our global gyrokinetic code GKNET [8] with kinetic electron dynamics [9]. We found that ITG/TEM turbulence can drive ion particle pinch by $E \times B$ drift $(n \neq 0)$ when the ion temperature gradient is steep enough. Electron particle pinch by $E \times B$ drift $(n \neq 0)$ is also driven in the case with the steep electron temperature gradient. Such an electron particle pinch can trigger an ambipolar electric field, leading to up-down asymmetric density perturbations and resultant ion particle pinch by not only magnetic drift but also $E \times B$ drift (n = 0). These results suggest that a density peaking of bulk ion due to turbulent fluctuations can be achieved by sufficiently strong both ion and electron heating.

To extend the above analysis in this paper, we investigate the balance of fuel supply and helium ash exhaust by including helium as an additional species. Unlike some simplified transport models, the full-f gyrokinetic model enables us to simulate flux-driven turbulence consistently coupled with a neoclassical transport mechanism, which is a novelty of this work. Furthermore, we examine the impact of helium to bulk ion temperature ratio, i.e. T_{z0}/T_{i0} , on the balance of fuel supply and helium ash exhaust in future burning plasmas.

The rest of this paper is organized as follows. In Sec. 2, we present the numerical model of GKNET used in our simulations. In Sec. 3.1, the simulation setting is described. The effect of ion/electron heating on the balance of fuel supply and helium ash exhaust is shown in Sec. 3.2. Then, we discuss the impact of helium to bulk ion temperature ratio in Sec. 3.3. Finally, the summary and some future plans are given in Sec. 4.

NUMERICAL MODEL OF GKNET CODE

The 5D full-f gyrokinetic code GKNET calculates the time evolution of gyro-center distribution function f_s of particle species $s \equiv i, e, He$ governed by the gyrokinetic Vlasov equation

$$\frac{\partial}{\partial t}(\mathcal{J}f_s) + \mathcal{J}\frac{d\mathbf{R}}{dt} \cdot \frac{\partial f_s}{\partial \mathbf{R}} + \mathcal{J}\frac{dv_{\parallel}}{dt}\frac{\partial f_s}{\partial v_{\parallel}} = \mathcal{J}C_{s,s} + \mathcal{J}S_{src} + \mathcal{J}S_{snk},\tag{1}$$

$$\frac{d\mathbf{R}}{dt} = \frac{1}{B_{\parallel s}^*} \left[v_{\parallel}(\mathbf{\nabla} \times \mathbf{A}) + \frac{B_0}{\Omega_s} v_{\parallel}^2(\mathbf{\nabla} \times \mathbf{b}) + \frac{c}{e_s} H_s \mathbf{\nabla} \times \mathbf{b} - \frac{c}{e_s} \mathbf{\nabla} \times (H_s \mathbf{b}) \right], \tag{2}$$

$$\frac{dv_{\parallel}}{dt} = -\frac{1}{m_{s}B_{\parallel s}^{*}} \left[(\nabla \times \mathbf{A}) \cdot \nabla H_{s} + \frac{B_{0}}{\Omega_{s}} v_{\parallel} \nabla \cdot (H_{s} \nabla \times b) \right], \tag{3}$$

where $\mathbf{R} \equiv (r,\theta,\zeta)$ is the position of guiding center, v_{\parallel} is the parallel velocity along the magnetic field line, μ is the magnetic moment, $\mathcal{J} \equiv rRB_{\parallel}^*$ is the phase space Jacobian. $\mathbf{B}_{\parallel,s}^* \equiv \nabla \times \mathbf{A}^* = \nabla \times (\mathbf{A} + B_0 v_{\parallel}/\Omega_s \mathbf{b})$ is the modified magnetic field for particle species s, $\mathbf{B} \equiv \nabla \times \mathbf{A} = (0, r/qR, R_0/R)B_0$ is the magnetic field for a circular concentric tokamak configuration with the safety factor q, $R = R_0 + r\cos\theta$ is the major radius, and $\mathbf{b} \equiv \mathbf{B}/B$, c is the speed of light, m_s , e_s and $\Omega_s \equiv e_s B_0/m_s c$ are the mass, the charge and the gyro frequency of particle species s, respectively. During the evolution of the distribution function, the phase space volume conservation

$$\frac{\partial}{\partial \mathbf{R}} \cdot \left(\mathcal{J} \frac{d\mathbf{R}}{dt} \right) + \frac{\partial}{\partial v_{\parallel}} \left(\mathcal{J} \frac{dv_{\parallel}}{dt} \right) = 0, \tag{4}$$

is satisfied because Eqs. (2)-(3) are analytically derived from the gyrokinetic Hamiltonian $H_s = m_s v_{\parallel}^2/2 + \mu B + e_s \langle \phi \rangle_s$, where $\langle \phi \rangle_s$ is the gyro-averaged electrostatic potential. In addition, exact particle conservation is kept including the magnetic axis by utilizing the gauge transformation technique to Eqs. (2)-(3). These properties are important for keeping numerical accuracy and stability in full-f gyrokinetic simulations.

The self-collision operator $C_{s,s}$ is modelled by the linear Fokker-Planck one [10] incorporated with the field particle operator [11] to conserve density, momentum and energy at each real space grid. Heat source and energy sink operators for species s are given by

$$S_{src,s} = A_{src}(r)\tau_{src}^{-1} [f_{M,s}(n_{s0}, 2T_{s0}) - f_{M,s}(n_{s0}, T_{s0})],$$
(5)

$$S_{snk.s} = A_{snk}(r)\tau_{snk}^{-1}[f_s - f_s(t=0)], \tag{6}$$

where $A_{src}(r)$ and $A_{snk}(r)$ are the deposition profiles, τ_{src} and τ_{snk} are the characteristic time of the heat source and energy sink operators.

$$f_{M,s}(n,T) = \frac{n}{\sqrt{2\pi T^3/m_s^3}} \exp\left[-\frac{m_s v_{\parallel}^2/2 + \mu B}{T}\right],\tag{7}$$

is the local Maxwellian distribution function with a density n, and a temperature T. n_{s0} , $v_{ts0} = \sqrt{T_{s0}/m_s}$, T_{s0} are the initial density, thermal velocity, and temperature at the half minor radius $r = a_0/2$ for species s. Equations (5) provides constant heat source, while there is no particle supply. On the other hand, Eq. (6) represents a simple model of energy sink at the plasma boundary by means of a Krook-type operator, which modifies the distribution function towards its initial profile at the outer boundary region [12].

The gyrokinetic Vlasov Equation (1) is coupled with the gyrokinetic quasi-neutrality conditions based on the hybrid kinetic electron model [9, 13, 14] given by

$$e_i \delta n_i + e_{He} \delta n_{He} + e_e \delta n_e = 0, \tag{8}$$

$$\delta n_i = \iint \langle \delta f_i \rangle_i \frac{B_{\parallel}^*}{m_i} d\nu_{\parallel} d\mu + \frac{1}{4\pi e_i} \nabla_{\perp} \cdot \frac{\rho_{ti}^2}{\lambda_{Di}^2} \nabla_{\perp} \phi, \tag{9}$$

$$\delta n_{He} = \iint \langle \delta f_{He} \rangle_{He} \frac{B_{\parallel}^*}{m_{He}} dv_{\parallel} d\mu + \frac{1}{4\pi e_{He}} \nabla_{\perp} \cdot \frac{\rho_{tHe}^2}{\lambda_{DHe}^2} \nabla_{\perp} \phi, \tag{10}$$

$$\delta n_{e,(m,n)=(0,0)} = \iint \left\langle \delta f_{e,(m,n)=(0,0)} \right\rangle_e \frac{B_{\parallel}^*}{m_e} d\nu_{\parallel} d\mu, \tag{11}$$

$$\delta n_{e,(m,n)\neq(0,0)} = \iint \left\langle \delta f_{e,t,(m,n)\neq(0,0)} \right\rangle_e \frac{B_{\parallel}^*}{m_e} dv_{\parallel} d\mu - \frac{\alpha_p n_e e_e \phi_{(m,n)\neq(0,0)}}{T_e}, \tag{12}$$

where $\rho_{ts} \equiv v_{ts}/\Omega_s = \sqrt{T_s/m_s}/(eB_0/m_sc)$, $\lambda_{Ds} = \sqrt{T_s/4\pi n_s e_s^2}$, n_s and T_s are the gyro radius, the Debye length, the density and temperature for species s, respectively. In Eqs. (9) and (10), Tayler expansion is used for the polarization densities, which have a stabilization effect on high wave-number modes. In this study, the most unstable mode is located around $k_\theta \rho_{ti0} \sim 0.3$, so that we believe it is acceptable to use the Tayler expansion, which is also supported by the mixing length estimate of the turbulent particle and heat transport. Second term of Eq. (12) denotes the adiabatic passing electron response with $(m,n) \neq (0,0)$, where α_p is the flux-surface averaged fraction of passing electrons given by

$$\alpha_p = 1 - \int_0^{2\pi} \sqrt{\frac{r(1 + \cos \theta)}{R}} \frac{R}{2\pi R_0} d\theta, \tag{13}$$

in a circular concentric tokamak case. $\delta f_{e,t}$ is the perturbed trapped electron distribution function, which satisfies $m_e v_\parallel^2/2 + \mu B < \mu B_{max}$. Here, B_{max} is the maximum magnetic field on a magnetic surface. Since both whole the trapped electron and (m,n)=(0,0) passing electron are treated as kinetic ones in this hybrid kinetic electron model, we can address TEM driven turbulence in addition to kinetic electron effects on neoclassical dynamics. Note that the components with $m \neq 0, n = 0$ are finite so that the radial $E \times B$ drift with n = 0 is precisely considered, which is one of the novelties in this study.

Here, we briefly describe numerical methods used in the GKNET code. The spatial derivatives in Eq. (1) are discretized by using the fourth-order Morinishi scheme [15, 16] and the time integration is performed using the fourth-order explicit Runge-Kutta method. The magnetic field B is calculated from the vector potential A by using the fourth-order finite difference method to numerically satisfy the phase space conservation given by Eq. (4). In this version of GKNET, we use 3D MPI decomposition for the (r, θ, μ) domain. Equation (8) is 1D Fourier-transformed along the ζ direction and then 1D Fourier-transformed along the θ direction after MPI_ALLtoALL transpose between the θ and ζ directions. Then by using MPI_ALLtoALL transpose between the r and θ directions again, we can solve Eq. (8) in the $(r, k_{\theta}, k_{\zeta})$ space, which has a tri-diagonal matrix form by applying the fourth-order finite difference method to the r direction. The matrix is not decomposed along the r direction so that LU decomposition can be directly applied without any MPI communications. In order to directly evaluate gyro-averaging for $\langle \delta f_s \rangle_s$ and $\langle \phi \rangle_s$, we make the 2D local

Polynomial interpolation on the poloidal plane to calculate the electrostatic potential on a gyro ring and then take 20 sampling points average in real space.

3. FULL-F FLUX-DRIVEN ITG/TEM SIMULATION FOR FUEL SUPPLY AND HELIUM ASH EXHAUST

In this section, we first describe the simulation settings in Sec. 3.1. In Sec. 3.2, we present the obtained density profiles and the time evolution of the particle fluxes for the case with thermalized helium $(T_{He0}/T_{i0} = 1)$. We also discuss the effect of electron heating on fuel supply and helium ash exhaust. Finally, we investigate the impact of helium to bulk ion temperature ratio by checking the case of non-thermalized helium $(T_{He0}/T_{i0} = 4)$.

3.1. Simulation setting

In this paper, we consider a circular concentric tokamak configuration with $a_0/R_0 = 0.36$ and $a_0/\rho_{ti0} = 100$, where $\rho_{ti0} \equiv v_{ti0}/\Omega_i$ are the ion radius at $r = a_0/2$. The initial background profiles are given by

$$n_s(t=0,r) = n_{s0} \exp\left[-\frac{0.3a_0}{L_n} \tanh\left(\frac{r-0.5a_0}{0.3a_0}\right)\right],\tag{14}$$

$$T_s(t=0,r) = T_{s0} \exp\left[-\frac{0.3a_0}{L_{T_s}} \tanh\left(\frac{r-0.5a_0}{0.3a_0}\right)\right],$$
 (15)

where $L_{n_s} \equiv -n_s/(dn_s/dr)$ and $L_{T_s} \equiv -T_s/(dT_s/dr)$ denote the typical scale lengths of initial electron and helium density gradients and temperature gradients at $r = a_0/2$. In this study, we set $R_0/L_{ne} = R_0/L_{nHe} = 2.22$ in all simulations. The initial ion density profile is determined by charge neutrality at t = 0 given by $e_i n_i (t = 0, r) + e_{He} n_{He} (t = 0, r) + e_e n_e (t = 0, r) = 0$. To investigate the impact of electron temperature gradient on particle flux, here we consider two cases. In the first case, both ion and electron temperature profiles are steep, which gradients are given by $R_0/L_{T_i} = R_0/L_{T_e} = 10$. Here, external ion and electron heat sources are introduced near the magnetic axis to maintain these steep temperature profiles (see Fig. 2 (a)). In the second case, only ion temperature is steep as $R_0/L_{T_i} = 10$, while electron temperature profile is set to $R_0/L_{T_e} = 4$. In this case, only ion heat source is introduced. The normalized self-collision frequencies are set to $v_{ii}^* = v_{ee}^* = v_{HeHe}^* = 0.025$ at $r = a_0/2$. To reduce the computational cost, the mass ratio between ion and electron is assumed to be $m_i/m_e = 100$. The other parameters are fixed as $m_{He}/m_i = 4$, $e_{He}/e_i = 2$, $e_i/e_e = -1$, $n_{i0}/n_{e0} = 0.9$, $n_{He0}/n_{e0} = 0.025$, and $T_{i0}/T_{e0} = 1$. Thermalized helium $(T_{He0}/T_{i0} = 1)$ is assumed in Sec. 3.2, whereas non-thermalized helium $(T_{He0}/T_{i0} = 4)$ is considered to assess its impact in Sec. 3.3.

Figure 1 (a) shows the radial profile of initial electron and helium densities, initial temperature with gentle gradient $(R_0/L_{T_s}=4)$ and steep gradient $(R_0/L_{T_s}=10)$. Safety factor profile is same as the standard cyclone-base-case as is shown in Fig. 1 (b).

From some convergence tests, simulation parameters are chosen as follows; the time step width is $\Delta t = 5 \times 10^{-4} R_0/v_{t0i}$, the grid number and the system size are $\left(N_r, N_\theta, N_\zeta, N_{v_\parallel}, N_\mu\right) = (64,192,48,64,16)$ and $\left(L_r, L_\theta, L_\zeta, L_{v_\parallel}, L_\mu\right) = (100 \rho_{ti0}, 2\pi, \pi/2, 10 v_{ts0}, 12.5 m_i v_{ts0}^2/B_0)$, respectively. In order to reduce the computational cost, the simulation domain is assumed to be an 1/4 wedge torus.

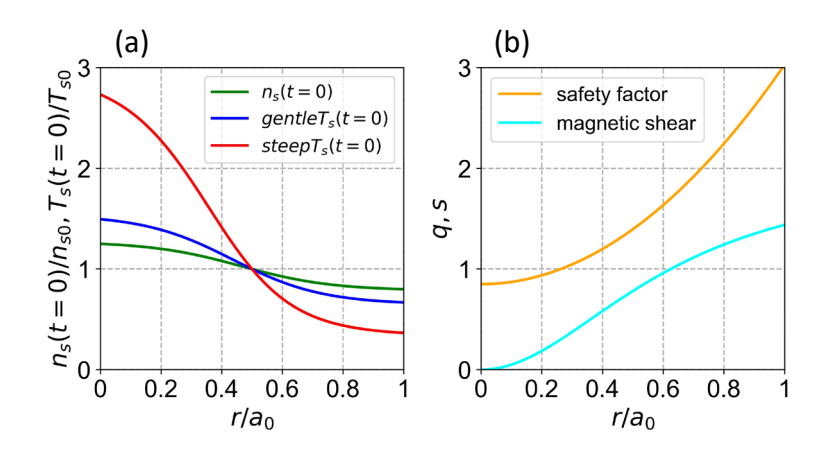


Figure 1. (a) The radial profiles of initial electron and helium densities (green), initial temperature with gentle gradient $(R_0/L_{T_s} = 4, blue)$ and steep gradient $(R_0/L_{T_s} = 10, red)$. (b) Safety factor (yellow) and the corresponding magnetic shear (light blue) profiles.

3.2. The effect of ion/electron heating on the ion density peaking and flattening

Figure 2 (a) shows the bulk ion density profiles after the nonlinear saturation in the two flux-driven ITG/TEM simulations, which initial temperature gradients are given by $(R_0/L_{T_l}, R_0/L_{T_e}, R_0/L_{T_{He}}) = (10, 10, 10)$ under both ion and electron heating, and $(R_0/L_{T_l}, R_0/L_{T_e}, R_0/L_{T_{He}}) = (10, 4, 10)$ under ion heating, respectively. The deposition profiles of applied heat source and energy sink are also shown. It is found that clear bulk ion density peaking is found to be observed in the ion/electron heating case, while density profile is weakly relaxed in the ion heating case. The temporal evolutions of non-axisymmetric and axisymmetric turbulent ion particle fluxes in the ion/electron heating and ion heating cases are shown in Fig. 2 (b) and (c), respectively. As was found from the flux-driven ITG/TEM simulations in the absence of impurities [7], ion heating can drive turbulent ion particle pinch by $E \times B$ drift $(n \neq 0)$ (see the red lines in Fig. 2 (b) and (c)) because the negative thermo-diffusion term becomes dominant. Turbulent electron particle pinch is also driven in the case with steep electron temperature gradient. Such an electron particle pinch can trigger an ambipolar field, leading to up-down asymmetric density perturbations and resultant ion particle pinch by not only magnetic drift but also $E \times B$ drift (n = 0) (see the blue line in Fig. 2 (b)). These results suggest that a density peaking of bulk ion due to turbulent fluctuations can be achieved by sufficiently strong both ion and electron heating even in the presence of impurities.

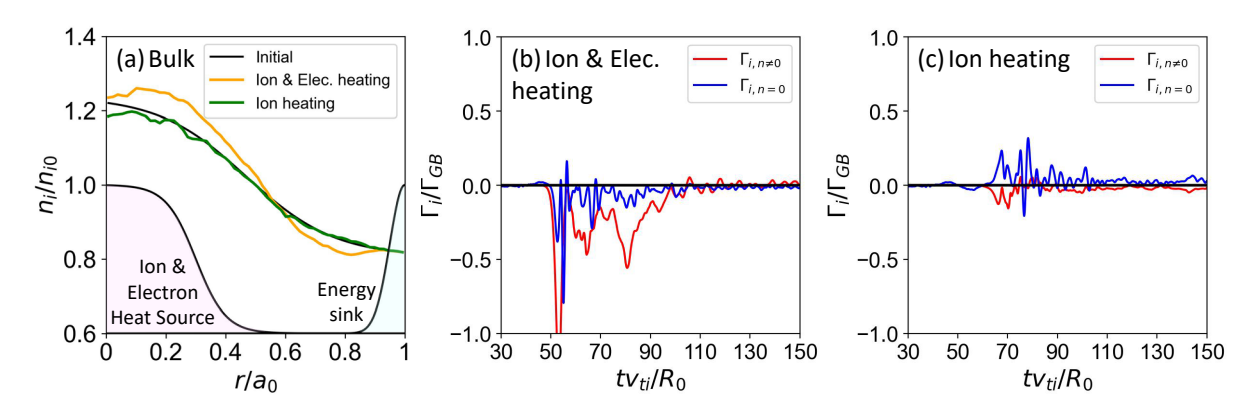


Fig. 2: (a) Bulk ion density profiles after the nonlinear saturation ($tv_{ti}/R_0 = 150$) in the ion/electron heating (yellow), and ion heating (green) cases, respectively. Temporal evolutions of non-axisymmetric (red) and axisymmetric (blue) turbulent ion particle fluxes in the (b) ion/electron heating and (c) ion heating cases. The particle fluxes are spatially averaged among $0.4a_0 < r < 0.6a_0$.

Figure 3 (a) shows the helium density profiles after the nonlinear saturation in the two flux-driven ITG/TEM simulations. The temporal evolutions of non-axisymmetric and axisymmetric turbulent particle fluxes of helium in the ion/electron heating and ion heating cases are also shown in Fig. 3 (b) and (c), respectively. It is found

that turbulent particle flux of helium by non-axisymmetric radial drift can provide helium ash exhaust (see the red lines in Fig. 3 (b) and (c)) contrary to the tendency of turbulent particle flux of bulk ion. Such a trend has been demonstrated not only by a quasilinear model and local δf gyrokinetic simulations [17], but also by full-f simulations [6]. However, particle flux of helium by the axisymmetric component is found to become negative in the ion/electron heating case (see the blue lines in Fig. 3 (b)) because turbulent particle transport triggers up-down asymmetric density perturbations, which in turn enhance the Banana-Plateau flux. Note that such a contribution is not considered in local and global δf simulations. As a result, these two fluxes cancel with each other and the total net particle flux of helium becomes small in the ion/electron heating case. By contrast, in the ion heating case, the particle flux of helium by the axisymmetric component is weakly positive, leading to helium ash exhaust.

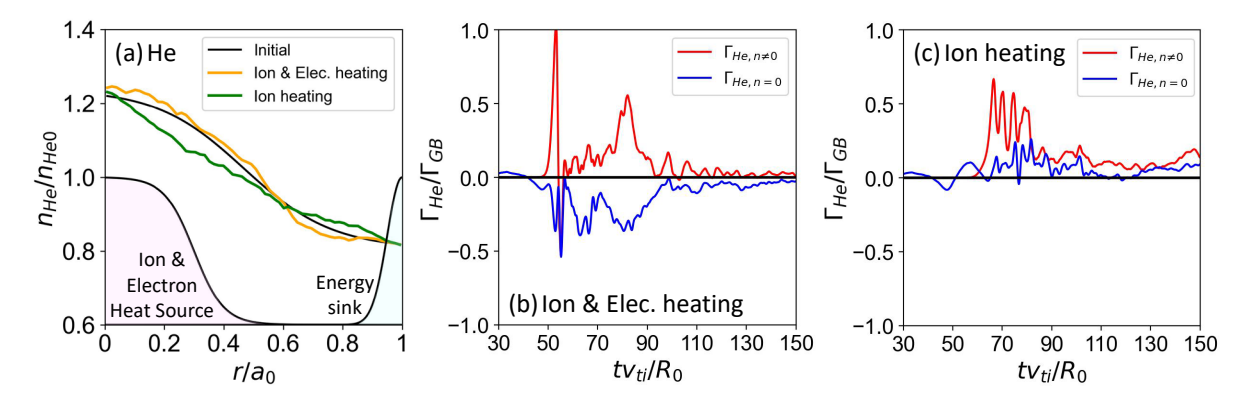


Fig. 3: (a) Helium density profiles after the nonlinear saturation ($tv_{ti}/R_0 = 150$) in the ion/electron heating (yellow), and ion heating (green) cases, respectively. Temporal evolutions of non-axisymmetric (red) and axisymmetric (blue) turbulent particle fluxes of helium in the (b) ion/electron heating and (c) ion heating cases. The particle fluxes are spatially averaged among $0.4a_0 < r < 0.6a_0$.

3.3. IMPACT OF HELIUM TO BULK ION TEMPERATURE RATIO

Then, we change the temperature ratio of helium to bulk ion; T_{He0}/T_{i0} . Figure 4 shows (a) bulk ion and (b) helium density profiles after nonlinear saturation in the ion/electron heating case with $T_{He0}/T_{i0} = 1$ and $T_{He0}/T_{i0} = 4$. Note that the yellow lines in Fig. 4 (a) and (b) are same as those in Fig. 2 (a) and Fig. 3 (a). Once the helium temperature increases, turbulent particle pinch of bulk ion by non-axisymmetric radial drift tends to be smaller (see the red line in Fig. 4 (c)) because the ITG instability is weakened by the increase of T_{He0} . Particle pinch of helium by the axisymmetric component is almost unchanged because turbulent electron particle pinch by non-axisymmetric radial drift also decreases, leading to an ambipolar field at nearly the same level.

On the other hand, turbulent particle flux of helium by non-axisymmetric radial drift tends to become negative (see the red line in Fig. 4(d)) due to the phase shift of helium density perturbation, which leads to the helium density peaking (see the purple line in Fig. 4 (b)). Figure 5 shows the net particle pinch of bulk ion and helium normalized by that in the case with $T_{He0}/T_{i0}=1$. This result demonstrates that the hot helium, i.e. higher T_{He0}/T_{i0} can prevent both fuel supply and helium ash exhaust, indicating the temperature ratio of helium to bulk ion is one of the key parameters for their control.

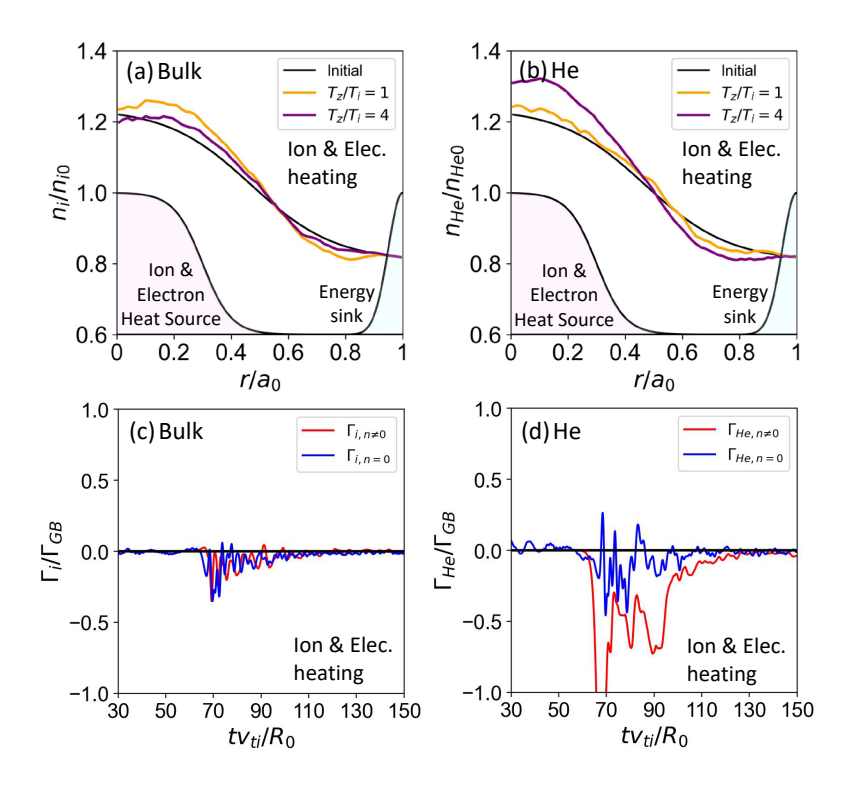


Fig. 4: (a) Bulk ion $n_i(r)$ and (b) helium $n_{He}(r)$ density profiles after the nonlinear saturation ($tv_{ti}/R_0 = 150$), where initial temperature gradients are given by $(R_0/L_{T_i}, R_0/L_{T_e}, R_0/L_{T_e}) = (10, 10, 10)$ under ion and electron heating with $T_{z0}/T_{i0} = 1$ (yellow) and $T_{z0}/T_{i0} = 4$ (purple). Temporal evolutions of non-axisymmetric (red) and axisymmetric (blue) turbulent particle fluxes of (c) bulk ion and (d) helium in the ion/electron heating case. The particle fluxes are spatially averaged among $0.4a_0 < r < 0.6a_0$.

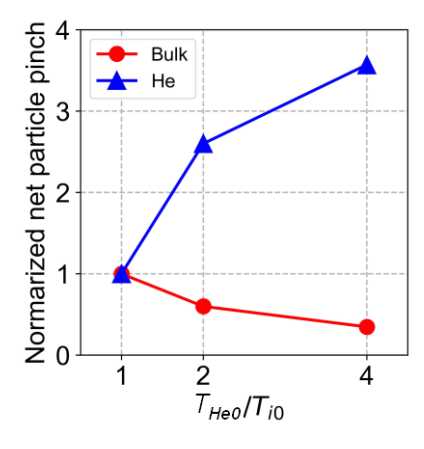


Fig. 5: Net particle pinch of bulk ion (red) and helium (blue) normalized by that in the case with $T_{z0}/T_{i0} = 1$. Initial temperature gradients are given by $\left(R_0/L_{T_i}, R_0/L_{T_e}, R_0/L_{T_z}\right) = (10, 10, 10)$ under ion and electron heating.

4. SUMMARY

We have performed flux-driven ITG/TEM simulations to study the balance of fuel supply and helium ash exhaust by means of our full-f gyrokinetic code GKNET with hybrid electron model. It is found that the temperature ratio of helium to bulk ion, i.e. T_{He0}/T_{i0} is one of the key parameters to control both fuel supply and helium ash exhaust. For thermalized helium $T_{He0}/T_{i0} = 1$, we observe clear turbulent particle pinch of bulk ion in the ion-electron heating case. Ion heating can drive turbulent ion particle pinch by non-axisymmetric drift. In addition, electron heating can also drive turbulent electron particle pinch, which can trigger an ambipolar electric field, leading to additional ion particle pinch by axisymmetric drift. On the other hand, the net helium flux is found to be relatively small because the enhanced negative Banana-Plateau helium flux cancels with the positive turbulent helium flux. For non-thermalized helium $T_{He0}/T_{i0} = 4$, such a turbulent ion pinch is found to be weakened and helium ash accumulation occurs because turbulent helium flux by non-axisymmetric radial drift tends to become negative. This means that hot helium can prevent both fuel supply and helium ash exhaust.

As future plans, larger plasma-size simulations with realistic mass ratio will be performed to confirm the observed mechanism can be active in future reactors. Isotopic electron heating has been identified as a candidate for controlling particle transport [18], and is also included in our future research plans. To study edge impurity accumulation, we will also perform full-f simulation with outer-core region by means of the new version of GKNET with field aligned coordinate [19].

ACKNOWLEDGEMENTS

Authors would like to thank Dr. Mikiya Muto in Kyoto University for his valuable comments on this study. The simulations were performed on the JFRS-1 in IFERC-CSC, the Plasma Simulator in NIFS. This work was supported by the JSPS KAKENHI Grant Number 24K06992, and the Joint Special Design Team Collaborative Research Program (06K055, 07K061).

REFERENCES

- [1] H. Nordman, J. Weiland, and A. Jarmen, Nucl. Fusion 30, 983-996 (1990).
- [2] C. Angioni, A. G. Peeters, X. Garbet, A. Manini, F. Ryter, and ASDEX Upgrade Team, Nucl. Fusion 44, 827-845 (2004).
- [3] C. Angioni, E. Fable, M. Greenwald, M. Maslov, A. G. Peeters, H. Takenaga, and H. Weisen, Plasma Phys. Control. Fusion **51**, 124017 1-14 (2009).
- [4] C. Angioni, Plasma Phys. Control. Fusion 63, 073001 1-22 (2021).
- [5] D. Estève, Y. Sarazin, X. Garbet, V. Grandgirard, S. Breton, P. Donnel, Y. Asahi, C. Bourdelle, G. Dif-Pradalier, C. Ehrlacher, C. Emeriau, Ph. Ghendrih, C. Gillot, G. Latu, and C. Passeron, Nucl. Fusion **58**, 036013 1-14 (2018).
- [6] Y. Idomura, K. Obrejan, Y. Asahi, and M. Honda, Phys. Plasmas 28, 012501 1-11 (2021).
- [7] K. Imadera, Y. Kishimoto, and A. Ishizawa, Nucl. Fusion 64, 086006 1-11 (2024).
- [8] K. Imadera, Y. Kishimoto, K. Obrejan, T. Kobiki, and J. Q. Li, "Global profile relaxation coupled with E × B staircase in toroidal flux-driven ITG turbulence", 25th Fusion Energy Conf. TH/P5-8 (2014).
- [9] K. Imadera and Y. Kishimoto, Plasma Phys. Control. Fusion 65, 024003 1-14 (2023).
- [10] G. Dif-Pradalier, P. H. Diamond, V. Grandgirard, Y. Sarazin, J. Abiteboul, X. Garbet, Ph. Ghendrih, G. Latu, A. Strugarek, S. Ku, and C. S. Chang, Phys. Plasmas 18, 062309 1-12 (2011).
- [11] S. Satake, R. Kanno, and H. Sugama, Plasma Fusion Res. 3, S1062 1-10 (2008).
- [12] Y. Idomura, H. Urano, N. Aiba, and S. Tokuda, Nucl. Fusion 49, 065029 1-14 (2009).
- [13] E. Lanti, B. F. McMillan, S. Brunner, N. Ohana, and L. Villard, J. Phys. 1125, 012014 1-11 (2018).
- [14] Y. Idomura, J. Comput. Phys. 313, 511-531 (2016).
- [15] Y. Morinishi, T. S. Lund, O. V. Vasilyev, and P. Moin, J. Comput. Phys. 143, 90-124 (1998).
- [16] Y. Idomura, M. Ida, T. Kano, N. Aiba, and S. Tokuda, Comput. Phys. Comm. 179, 391-403 (2008).
- [17] C. Angioni, F. J. Casson, C. Veth, and A. G. Peeters, Phys. Plasmas 19, 122311 1-8 (2012).
- [18] M. Nishiura, A. Shimizu, T. Ido, S. Satake, M. Yoshinuma, R. Yanai, M. Nunami, H. Yamaguchi, H. Nuga, R. Seki, K. Fujita, and M. Salewski, Phys. Plasmas 31, 062505 1-6 (2024).
- [19] S. Okuda, H. Seto, and K. Imadera, Plasma Fusion Res. 18, 403040 1-5 (2023).